crystals

MDPI

Article

Additive Manufacturing of Piezoelectric Niobium-Doped Lead Zirconate Titanate (PZT-N) by Binder Jetting

Marco Mariani [1], Elisa Mercadelli [2,*], Laura Cangini [2,†], Carlo Baldisserri [2], Carmen Galassi [1,2], Claudio Capiani [2] and Nora Lecis [1]

[1] Department of Mechanical Engineering, Politecnico di Milano, 20156 Milano, Italy; marco.mariani@polimi.it (M.M.); carmen.galassi@issmc.cnr.it (C.G.); nora.lecis@polimi.it (N.L.)
[2] National Research Council of Italy, Institute of Science, Technology and Sustainability for Ceramics (CNR-ISSMC, former ISTEC), 48018 Faenza, Italy; carlo.baldisserri@issmc.cnr.it (C.B.); claudio.capiani@issmc.cnr.it (C.C.)
* Correspondence: elisa.mercadelli@issmc.cnr.it
† Current address: Department of Materials and Earth Sciences, Technical University of Darmstadt, 64287 Darmstadt, Germany.

Abstract: Binder jetting is an emerging indirect additive manufacturing technique for ceramic materials, which could be employed to produce application-oriented designed components impossible to achieve with traditional processes and featuring enhanced performances. In our study, niobium-doped lead zirconate titanate (PZT-N) powder, usually processed through the standard press-and-sinter route, was employed as the raw material. First, the powder was characterized in terms of granulometry and flowability to assess its suitability for the printing process. Then, shaping by binder jetting was studied, and the effect of three levels of binder saturation (75–90–105%) on the green bodies was assessed. Finally, the microstructure of the sintered samples was studied using SEM, to investigate the effect of thermal treatments on the grain size distribution and residual porosity (~40%). The piezoelectric properties were measured and compared to those of conventionally processed material. The piezoelectric charge and voltage constants (d_{33} and g_{33}) were evaluated to determine the possible use of printed parts as porous piezoelectric components to be exploited in hydrophones in the direct mode.

Keywords: binder jetting; additive manufacturing; 3D printing; piezoceramic; porosity; lead zirconate titanate

Citation: Mariani, M.; Mercadelli, E.; Cangini, L.; Baldisserri, C.; Galassi, C.; Capiani, C.; Lecis, N. Additive Manufacturing of Piezoelectric Niobium-Doped Lead Zirconate Titanate (PZT-N) by Binder Jetting. *Crystals* **2023**, *13*, 883. https://doi.org/10.3390/cryst13060883

Academic Editors: Floriana Craciun and Haibo Zhang

Received: 28 April 2023
Revised: 24 May 2023
Accepted: 25 May 2023
Published: 27 May 2023

1. Introduction

Lead zirconate titanate ($PbZr_xTi_{1-x}O_3$, PZT) is the most widely studied and employed material in piezoelectric devices. Its ferroelectric properties are highly dependent on the composition close to the morphotropic phase boundary (MPB), the effects of dopants, and the influence of the microstructural properties achieved during shaping and densification [1–3]. Nonetheless, the use of lead is critical due to its poisoning effects, and its use has been limited to certain amounts and cases [4].

The need to reduce material consumption during the process of manufacturing high-efficiency devices has encouraged the search for innovative techniques, such as additive manufacturing (AM) methods, for PZT production with custom-oriented configurations and functional porosity [5–8]. However, applying AM to ceramics is still challenging, and complications arise when strict requirements are set on both structural and functional properties, as in the case of piezoelectric materials [9]. As reported in Table 1, most previous works have employed indirect AM techniques, in particular, fused-filament fabrication (FFF) [10–15], stereolithography (SLA) [16–18], direct ink writing (DIW) [19,20], and binder jetting (BJT) [21], because they allow the required sintering treatments to be performed separately from the shaping phase with a fine control on the thermal cycle and, thus,

on the microstructural evolution. On the contrary, direct AM routes, such as selective laser sintering (SLS) [22,23] and laser-engineered net shaping (LENS) [24], have the main advantage of providing final products right after printing, but they do not offer a tight control on the heating, sintering atmosphere, and cooling rate during processing. Therefore, the microstructure may suffer from a series of defects, such as phase composition variations, cracking, texturing, and grain coalescence, which can only be partially solved with post-processing treatments such as annealing.

Table 1. State of the art on additive manufacturing of PZT-based components.

AM	Material	ρ	d_{33}	g_{33}	FoM_{33}	Notes	Ref.
		g cm^{-3}	pC N^{-1}	10^{-3} Vm N^{-1}	10^{-15} m^2 N^{-1}		
FFF	PLZT	-	412	78	32,126	-	[13,14]
	PZT	~8	202/273 *	77/26 *	15,554/7098 *	50% infill density	[15]
SLA	PZT-5H	~7.5	-	-	-	-	[16]
	PZT-5H	6.94	212	-	-		[17]
	PZT-5H	~6.9	525	-	-	Use of pore formers	[18]
DIW	PLZT	3.77	347	~90	~30,000	Epoxy matrix	[19]
	PZT Type VI	7.21	678	-	-	-	[20]
BJT	PZT	-	469/541 **	-	-	-	[21]
SLS	PZT	1.65	-	-	-	-	[22]
	PZT-19M+SiO_2	3.88	-	-	-	PVDF matrix	[23]
LENS	PZT	~7	-	-	-	-	[24]

* The first value refers to a scaffold structure, the second to an offset structure. ** The first value refers to the measurement in the parallel direction with respect to the layer's surface, the second one is measured in the perpendicular direction.

Among the indirect AM techniques, SLA seems the most reliable for manufacturing dense components with a reduced surface roughness; however, this process is a complex and inherently low-productivity one, in addition to having strict requirements for the photocurable slurry. On the other hand, FFF and DIW provide remarkable results with low-budget machines but pose limitations on the feasible designs, and their accuracy depends on the filament size and shape. BJT has the highest throughput, and its only theoretical geometrical limit is represented by closed cavities. In practice, thin details such as walls and channels of reduced diameter are challenging to produce. Nonetheless, the production of bulk components with a non-conventional configuration is simpler compared to conventional techniques based on powder processing, possibly combined with isostatic pressing. Indeed, shaping by BJT relies on a layer-by-layer approach where the particles are selectively joined by the deposition of a ligand from a printhead (Figure 1). The self-supporting mechanism of the powder bed permits the production of overhangs without the need for external support structures, which, combined with the possibility of producing intricate structures, potentially could allow lattice and metamaterial manufacturing without the need for post-processing operations (e.g., machining).

However, the use of dry powders for layer-by-layer deposition poses a series of challenges toward achieving a high green density and, as a consequence, full density after sintering, particularly for ceramic materials that do not feature liquid sintering [25–28].

In this work, the first comprehensive analysis of the production of PZT by BJT is presented. A detailed description of the relevant properties is given for the particulate feedstock, the printed parts, and the densified components. Similarly to previous works on sodium–potassium niobate (KNN) and barium titanate (BT), the focus is placed on the effects of the residual porosity in the final microstructure and on the piezoelectric properties of the manufactured parts [21,29–32]. The performance is compared to that of dense parts obtained by conventional methods and other techniques employed to produce porous piezoceramics [33–37].

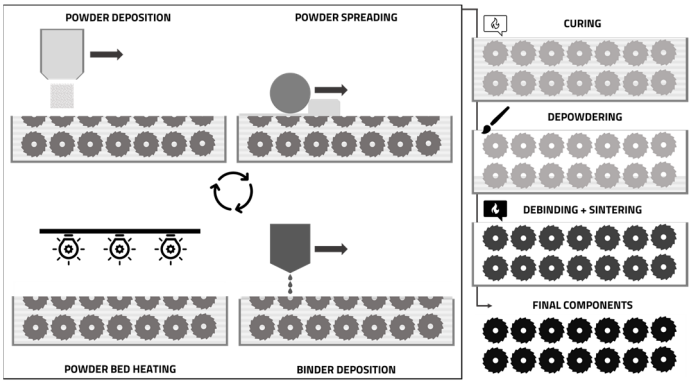

Figure 1. Representative scheme of the binder jetting process, comprising the shaping phase and thermal treatments.

2. Materials and Methods

2.1. Materials and Sample Preparation

The powder employed in the study had a nominal composition of $Pb_{0.988}[(Zr_{0.52}Ti_{0.48})_{0.976}Nb_{0.024}]O_3$ (PZT-N). Powder production by the solid-state reaction and its conventional processing via die pressing were optimized in previous studies [3]. In this work, the samples were shaped by binder jetting using an Innovent+ 3D printer by ExOne Inc (North Huntingdon, USA). The powder was dried at 120 °C for 2 h before printing to remove excess humidity and improve the flowability of the material. The liquid binder used to consolidate the green bodies was the aqueous-based solution (AquaFuse©) by ExOne, containing water, high-volatility solvents, and polyethylene glycol (PEG) precursors. The layer thickness was set at 50 µm and the binder saturation at 75–90–105%, respectively. The printed samples were disks with 25 mm diameter and 2.5 mm thickness.

The printed samples were cured at 180 °C for 6 h to crosslink the polymeric binder. Then, they were debinded at 470 °C for 4 h and, finally, sintered at 1200 °C or 1250 °C for 2 h.

2.2. Microstructural and Piezoelectric Characterizations

The powder morphology and the cross-section fracture surfaces were investigated using field emission-scanning electron microscopy (SEM, ZEISS SIGMA 500, Jena, Germany). The fracture surface was obtained in the perpendicular direction with respect to the surface of the powder layers.

The median dimension, the size distribution, and the circularity (i.e., the ratio between the actual perimeter of the particle section and the equivalent circle) of the particles were quantified using static image analysis granulometry according to ASTM E2651-19 (Malvern Morphology 4) with a resolution of 150 nm.

The flowability of the powder was evaluated by calculating the Hausner ratio from the apparent/tapped density and the dispensing rate, according to the procedure in [28]. Owing to the open porosity of the material, its densities at the green and sintered states were calculated using the geometrical method on disk-shaped samples. The grain size distribution curves were obtained by manually measuring at least 100 grains from the SEM images of the fracture surfaces.

X-ray diffraction (XRD) analyses on both the starting powder and the sintered samples were performed over the $20° \leq 2\theta \leq 80°$ range (step size 0.02°) at a scanning rate of 1° min-1 with Cu-Kα radiation (λ = 1.5406 Å) in a D8 ADVANCE, LynkEye detector, Bruker AXS, Massachusetts (USA).

The relative density values were calculated from a theoretical density of 8.006 g cm^{-3}. The mean pore size and distribution of the sintered samples was determined by mercury intrusion porosimetry (MIP, Autopore V9600, Norcross, GA, USA).

Silver electrodes were applied to the sintered samples, on the flat surfaces perpendicular to the printing directions. The PZT-N discs with the electrodes were then poled at 3 kV mm^{-1} in silicone oil at 120 °C for 40 min.

The piezoelectric properties were measured at room temperature by acquiring the piezoresonance spectra over the 100 Hz–40 MHz range (Hewlett Packard HP 4194A, Yokogawa, Japan), noting the resonance and anti-resonance frequencies in both radial and thickness modes. Piezoresonance frequency data were processed according to the 1986 ASTM standard on piezoelectricity. The capacitance and the loss tangent at 1 kHz were also measured.

Dielectric dispersion curves were obtained from the primary ($\left|\widetilde{Z}\right|$, $\phi\left(\widetilde{Z}\right)$) data. The magnitude and phase angle $|\widetilde{\varepsilon}_r|$, $\phi(\widetilde{\varepsilon}_r)$ of the complex relative dielectric constant $\widetilde{\varepsilon}_r$ were obtained using Equation (1)

$$\widetilde{\varepsilon}_R = \frac{d}{\varepsilon_0 A}\frac{1}{j\omega|Z|}e^{-j\phi} \quad (1)$$

where d and A are the thickness and the area of the samples, respectively; $\omega = 2\pi f$; and $\varepsilon_0 = 8.8542 \times 10^{-12}$ F m^{-1}. Ten (Z | and $\phi(Z)$ measurements were performed at each frequency, and the average values of both $|Z|$ and $\phi(Z)$ were used in Equation (1) to obtain $|\widetilde{\varepsilon}_r|$ and $\phi(\widetilde{\varepsilon}_r)$.

A d33-meter (Sinocera S 5865, Shanghai, China) was employed to evaluate the piezoelectric charge coefficient after calibration with a 360 pC N^{-1} standard sample provided by the manufacturer. The measurements were taken by clamping the specimens on the flat surfaces at different locations, and they were repeated multiple times for each sample under different conditions of temperature and residual humidity.

Finally, the measured parameters were used to calculate the figure of merit (FoM) for hydrophones and direct-mode (3–3) applications, respectively, in Equations (2) and (3) [38,39]:

$$d_h g_h = (d_{33} + 2d_{31})(g_{33} + 2g_{31}) \quad (2)$$

$$FoM_{33} = d_{33} g_{33} \quad (3)$$

3. Results and Discussion

3.1. Characterization of the Powder and Green Bodies

The powder was used in its as-synthesized state, so its morphology was irregular as shown in Figure 2. In addition, it can be observed that the particle size is in the range of hundreds of nanometers, which promotes the tendency to aggregate in micrometric agglomerates under the influence of short-range interactions such as Van der Waals and capillarity ones. The granulometric analysis confirmed these observations, as shown in Figure 3. A bimodal particle size distribution appears in Figure 3A, with a finer fraction displaying a mean size of 200 nm and a coarser one of 2 µm. In Figure 3B, it can be noticed that fine aggregates below 10 µm tended to retain a more compact shape with more pronounced sphericity with respect to isolated particles and coarse aggregates.

The packing behavior of the particles proved poor, with a Hausner ratio equal to 1.36 ± 0.08 (ρ_{app} = 19.58 ± 1.34%; ρ_{tap} = 24.90 ± 0.82%), due to the low median size combined with the high interparticle interactions, hindering reciprocal particle motion and, thus, the filling of voids. The dispensing rate was measured as 177.84 ± 48.65 mg cm^{-2} s^{-1} and 22.21 ± 6.08 mm^3 cm^{-2} s^{-1} for mass and volume flows, respectively. In addition to confirming the limited flowability of the feedstock, the large standard deviation values highlight the difficulty of achieving a repeatable flow in the printing apparatus, thus leading to the need to decrease the recoat speed to ensure the deposition of a sufficient amount of powder at each layer.

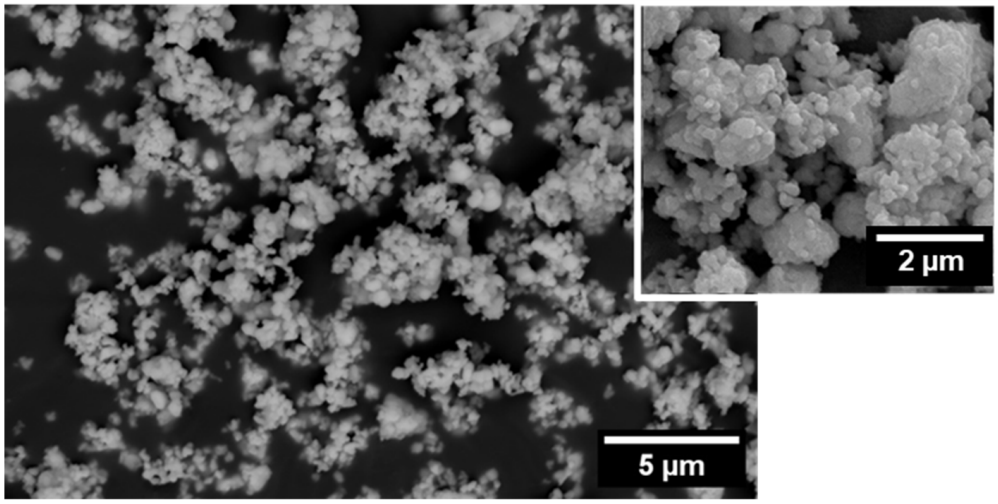

Figure 2. SEM image of the PZT-N powder.

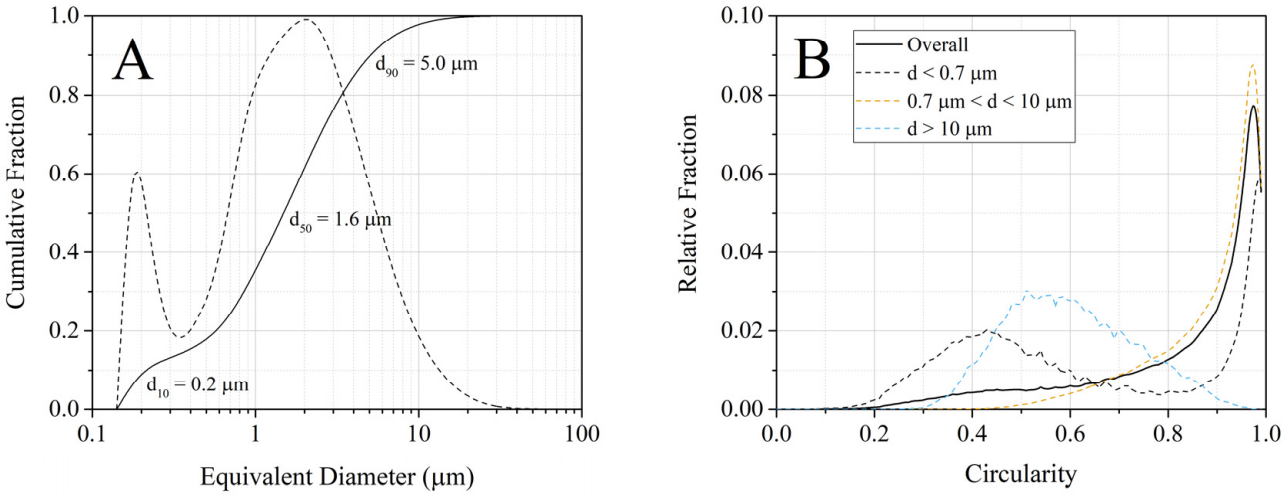

Figure 3. Number-based granulometry curves of the particles for (**A**) the size distribution and (**B**) the circularity index of the fractions below 700 nm, above 10 µm, and in between these values.

The poor flowability of the PZT-N powder is reflected in the limited green density of the samples, close to 20% regardless of binder saturation (Figure 4). Moreover, it can be observed that the oversizing of the samples (measured as the size variation with respect to the CAD file) was evident both along the planar surface (*d*) and the printing direction (*h*) and that it increased with greater binder saturation, especially in the first direction. The loose powder bed was characterized by macropores that generate a weak capillary pressure on the deposited binder, thus hindering the infiltration of the liquid; consequently, the ligand tended to spread laterally on the layer top surface, wetting an out-of-bounds portion of the powder bed. This mechanism was accentuated as the volumetric liquid fraction increased (binder saturation = 105%).

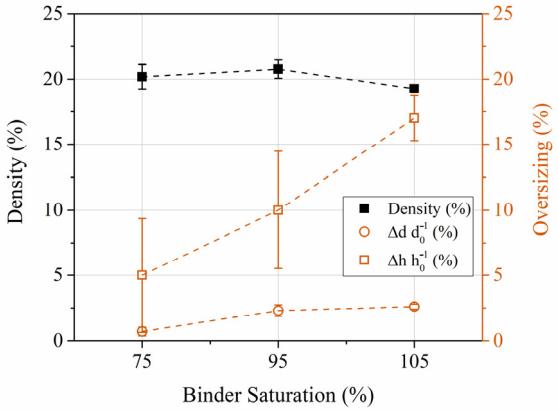

Figure 4. Values of relative green density (black) and oversizing (red) with respect to the CAD file along the diameter (*d*) and height (*h*) of the disk-shaped samples.

3.2. Microstructural Analysis of the Sintered Samples

The XRD analyses in Figure 5 confirm that complete calcination of the starting powder was achieved at both sintering temperatures, leading to the crystallization of the perovskitic PZTN phase, as underlined by the evolution of the diffraction peaks. In both conditions, the characteristic peaks associated with the formation of the monoclinic and tetragonal lattices were present, coherently with the presence of the morphotropic phase boundary (MPB) for this kind of composition. The more marked splitting of the peaks underlines that, at 1250 °C, the tetragonal phase increased at the expense of the monoclinic one [36].

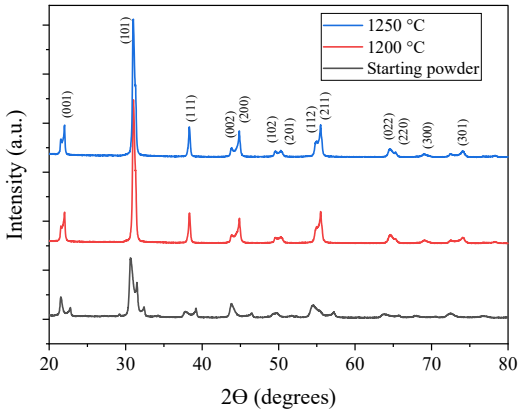

Figure 5. XRD spectra of the starting powder (black) and samples sintered at 1200 °C (red) and 1250 °C (blue).

The values reported in Figure 6 show that the material experienced a noticeable densification upon sintering, especially at 1250 °C. In this case, the average value was close to 60%; thus, the density roughly tripled during the treatment. The final density was not affected by binder saturation: the relative density registered after sintering at 1250 °C corresponded to 59.0 ± 0.1%, 58.4 ± 0.1%, and 59.2 ± 0.1% for binder saturation levels of 75%, 90%, and 105%, respectively. It is interesting to notice that the increased densification at the highest temperature seems to be correlated to the enhanced linear shrinkage in the building direction. Indeed, the reduction in the diameter was almost constant at ~30%, while the thickness shrank by ~20% and ~52% for the 1200 °C and 1250 °C sintering temperatures, respectively.

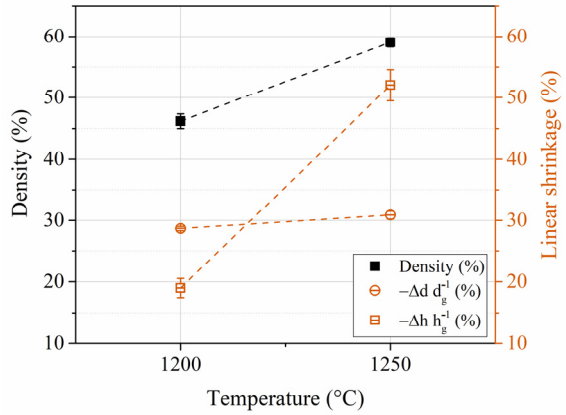

Figure 6. Values of relative sintered density (black) and linear shrinkage (red) with respect to the green dimensions (d_g and h_g) along the diameter (d) and height (h) of the disk-shaped samples from a binder saturation of 90%.

The porosity distribution in the green bodies is responsible for such a mechanism. In the case of poor packing of the powder bed resulting in decreased capillary suction, the binder accumulates at the interface between the layers, rather than infiltrating within them. Therefore, debinding-generated macroporosity tends to accumulate in such regions. In the case of enhanced volumetric diffusion mechanisms promoted by high sintering temperatures (i.e., 1250 °C), the material also fills the interlayer porosity, thus minimizing the separation among the layers and reducing the thickness of the sample—the latter being the sum of the thicknesses of layers and interlayers. When the sintering temperature is insufficient (e.g., 1200 °C), the densification only occurs within the layers. These have an intrinsic porosity dependent on the feedstock flowability, the powder bed spreading parameters and, to a lesser extent, on the binder infiltration, i.e., binder saturation. As stated above, in these cases, the effect of the binder on layer packing is negligible due to the poor imbibition of the powder bed.

The SEM micrographs of the samples sintered at 1250 °C (Figure 7) seem to confirm this hypothesis. The surface fracture of samples printed with the three binder saturation levels revealed a similar microstructure: the macroporosity was elongated and concentrated among layers, with a few solid bridges connecting them, while the microporosity was distributed within the densified regions (Figure 7B). It was still possible to identify the individual layers in most parts of the material, as indicated in Figure 7A–C: these correspond to highly densified regions of thickness close to 50 µm, developing in the direction parallel to the surface of the powder bed and delimited by large macropores. Microscopy (see Figure 7B) also revealed the presence of three orders of characteristic pore sizes: macroscopic voids of tens of micrometers in size, pores having a size in the range of a few micrometers, and nanometric porosity within dense regions.

Additional details on the microstructure of the samples can be observed from the grain and pore size distribution curves in Figure 8A and B, respectively. The mean grain size slightly increased with increasing binder saturation (Figure 8A), while the span of the distribution curve appeared to be constant throughout the samples. This growth was not correlated to the density of the samples, which was roughly constant across the three conditions. On the contrary, a clear distinction could be made on the basis of the pore size distribution for samples produced with 75, 90, and 105% binder saturation. In the latter case, the sample displayed a trimodal distribution with a significant cumulative fraction of macrovoids centered at 100 µm, which might be due to the excessive amount of binder deposited during printing that accumulates at the interface among layers (Figure 8B).

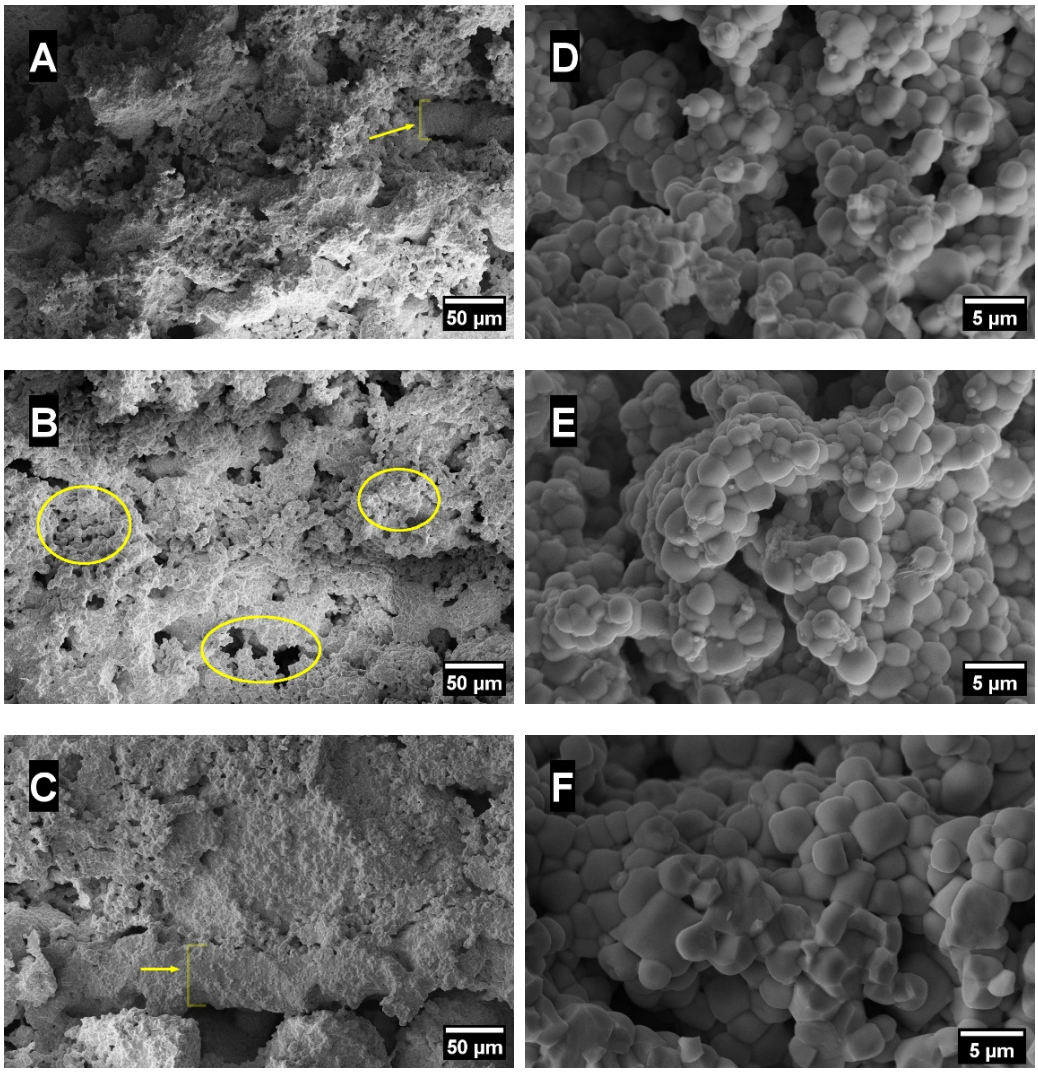

Figure 7. SEM images of the cross-section fracture surfaces of the samples sintered at 1250 °C manufactured with a binder saturation of (**A**,**D**) 75%, (**B**,**E**) 90%, and (**C**,**F**) 105%. The arrows indicate the highly densified individual layer; the circles evidence the different pore sizes in the sintered material.

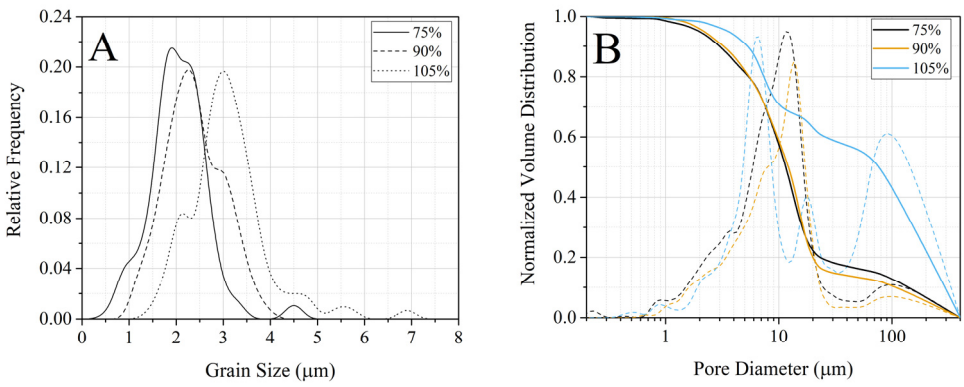

Figure 8. (**A**) Grain size and (**B**) pore size relative frequency distribution curves of the sample sintered at 1250 °C.

The microstructure of the sintered samples is a direct consequence of the heterogeneous distribution of the binder within the green bodies, as observed for other materials as well [40–43] and further highlighted by the shell printing strategy [44,45]. Regions featuring a high binder concentration have a larger porosity after debinding, and they experience a limited densification upon sintering; on the contrary, the dry volumes confined within these regions have a better packing and, thus, higher particle coordination numbers and diffusive paths at high temperatures. In the case of shell printing, such an effect is purposely obtained by depositing the binder only in the outer bound of the desired geometry; in our case, this effect was downscaled to each layer, due to ineffective infiltration of the liquid caused by the limited capillary suction.

3.3. Electric Impedance and Dielectric and Piezoelectric Properties of the Sintered Samples

The log–log graphs of the impedance (Figure 9A,B) displayed straight lines up to 1 MHz, which indicates that the samples behave as low-loss capacitors over the 10^2–10^6 Hz frequency range. All samples behaved as quasi-ideal capacitors up to frequencies of the order of 1 MHz, with values of $\phi(\varepsilon_r)$ close to zero (Figure 9D). The graph of the magnitude of the relative dielectric constant (Figure 9C) displayed a small discrepancy between the sample obtained at 105% binder saturation and the remaining samples: the value of the relative dielectric constant was lower (~400 vs. ~500) over the entire range of frequencies. Both values were coherent with the volume fraction of porosity, similar to magnitudes achieved through other techniques [3,35,36]. This parameter is sensitive to the internal porosity; thus, the different behavior is likely correlated to the pore size distribution, which featured a relevant volume fraction close to 100 µm for this specific printing condition (Figure 8B). Indeed, it is known that both the amount of porosity and its distribution/interconnectivity contribute to determining the electrical behavior of the material: a more pronounced 3–3 connectivity is associated with a lower dielectric constant, which, in our case, might occur in the presence of a larger fraction of macroscopic porosity [37].

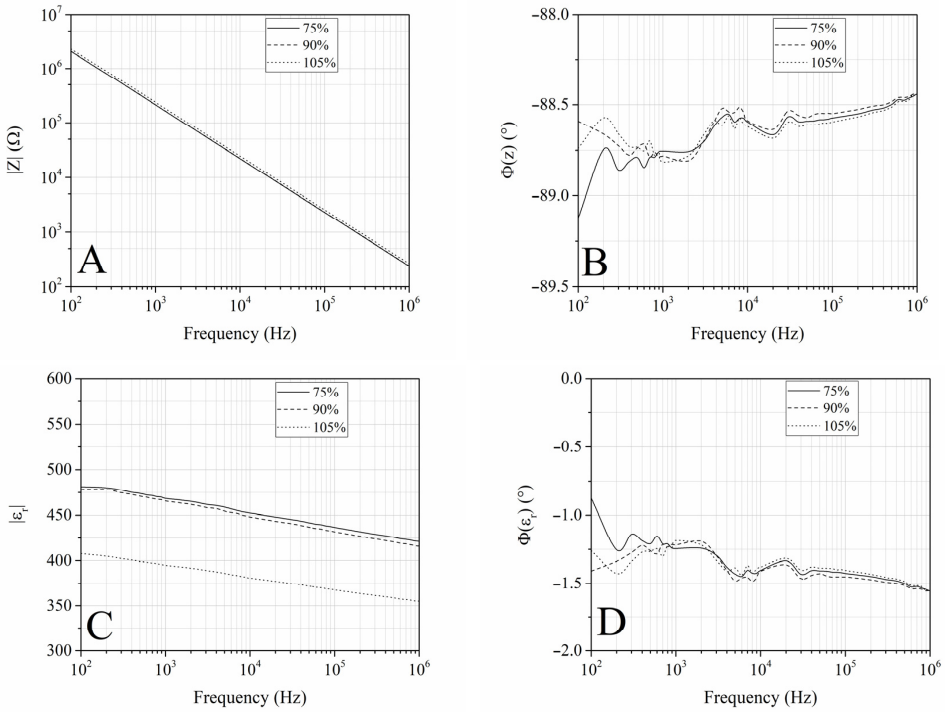

Figure 9. (**A**) Pre-poling impedance magnitude, (**B**) impedance phase angle, (**C**) relative dielectric constant magnitude, and (**D**) relative dielectric constant phase angle of the three disk-shaped samples under harmonic excitation over the 10^2 Hz ÷ 1 MHz frequency range.

It can be observed from Table 2 that the measured properties varied according to the degree of porosity introduced in the microstructure. Compared to the dense counterpart obtained by die-pressing, there was a consistent reduction in the electrical permittivity, the strain coefficient, the mechanical quality factor, and the acoustic impedance: this is consistent with the introduction of more than 40% of open porosity in the material, as already observed in the literature. Nonetheless, the sharp increase in the voltage coefficients (e.g., g_{33} was tripled) led to consistent increases in the correlated figure of merit. The values reported for our technique are impressive and they could provide optimal results in applications where the geometrical design freedom provided by AM, which can hardly be achieved by other techniques, is desired [6,46].

Table 2. Physical, dielectric, and piezoelectrical properties and figures-of-merit of porous PZT samples obtained by binder jetting (this work) compared to the dense specimen and the literature values.

Sample	p	${\varepsilon_{33}}^T$	k_p	$-k_{31}$	$-d_{31}$	d_{33}	$-g_{31}$	g_{33}	${s_{11}}^E$	Q_m	σ^E	${v_1}^E$	Z_a	$d_h g_h$	FoM_{33}
	g cm^{-3}				10^{-12} C N^{-1}		10^{-3} V Pa^{-1}		10^{-12} Pa^{-1}			m s^{-1}	10^6 kg m^{-2} s^{-1}	10^{-15} Pa^{-1}	10^{-15} Pa^{-1}
75%	4.72	482	0.28	0.16	93	319	22	75	81	18	0.33	1615	7.63	4137	23,925
90%	4.81	464	0.24	0.15	79	306	19	75	66	24	0.24	1770	8.51	5402	22,950
105%	4.65	400	0.23	0.13	71	291	20	82	79	24	0.33	1651	7.68	6194	23,862
Dense	8.00	1721	0.69	0.39	193	440	13	26	17	89	0.35	2773	22.2	0	11,440
[3]	3.68	62	0.13	0.08	23	97	41	91	162	72	0.3	1309	4.70	500	8554
[35]	4.95	404	0.17	0.04	15	202	4	57	43				10.70	8428	11,514
[38]	4.78	500		0.08	39	295	9	67						10,600	19,765
[47]	~3.5	~1500			~150	~670							~3	~9000	
[48]	5.6	~900	0.63		~125	~450									~20,000

Straightforward piezoeresonance data treatment according to the ASTM standard on piezoelectricity relies on the assumption that the physical behavior of the sample is akin to that of the piezo-elastic continuum, whose physical description is inherently linear. In the case of materials that display piezoelectric activity but whose structure is not continuous and homogeneous, the physical significance of the above data may be argued. All parameters appearing in Table 2 describe the properties of an equivalent piezo-elastic continuum which—cast in the shape of the samples analyzed in this work—yields piezoresonance data (resonance and anti-resonance frequencies in the thin-disk radial and thickness modes) such as those that were measured. While the results in Table 2 are physically reasonable and useful for the purpose of characterizing the materials' performance, issues such as the role of porosity and the textured structure that are the result of the AM process employed in the production of the samples—and their effect on the apparent piezoelectric constants—may require a more detailed investigation.

4. Conclusions

A comprehensive study on the manufacturing of PZT-N by BJT was presented for the first time.

The morphological characteristics of the starting PZT-N powders produced via a conventional solid-state reaction were deeply investigated. It was found that the starting feedstock presented poor flowability and packing behavior of the powder bed. Different binder saturation levels, i.e., 75, 90, and 105%, were considered. The results showed that the green (≈20%) and final (≈59%) densities of the obtained samples after sintering at 1250 °C were not affected by the binder saturation, due to the poor imbibition and capillary suction of the powder bed. Microstructural analyses of the sintered PZT-N samples confirmed a heterogeneous distribution of the binder within the green bodies that created elongated macroporosity among the layers, while microporosity was distributed within the densified regions. Pore size distribution curves confirmed the SEM data, evidencing, for the sample produced with 105% of binder saturation, the formation of a significant cumulative fraction of macrovoids due to the accumulation of the binder at the layers' interface.

Promising piezoelectric properties, consistent with the introduction of more than 40% of open porosity in the material, were registered for PZT-N manufactured by BJT.

Remarkable figures of merit (FoM), typically required for porous piezoceramics, were registered in this study. This work confirms that binder jetting is a valuable additive manufacturing technique to produce PZT-based piezoceramics directly from as-synthesized powders, with high geometrical design freedom and reduced material waste.

Author Contributions: Writing—original draft: M.M.; methodology: M.M., L.C. and C.C.; conceptualization: M.M. and N.L.; investigation: M.M., L.C., C.B. and C.C.; validation: E.M. and C.B.; supervision: E.M., C.G. and N.L.; writing—review and editing: E.M., L.C., C.B. and C.G.; project administration: N.L. All authors have read and agreed to the published version of the manuscript.

Funding: This research received no external funding.

Data Availability Statement: The data presented in this study are available on request from the corresponding author.

Acknowledgments: The authors would like to acknowledge the "Functional Sintered Materials (Funtasma)" Interdepartmental Laboratory of Politecnico di Milano, where this research activity was partially developed. Support by the Italian Ministry for Education, University, and Research through the project Department of Excellence LIS4.0 (Integrated Laboratory for Lightweight e Smart Structures) is also acknowledged. C.B. and L.C. acknowledge the support from the project "DIGIMAN—Soluzioni per la DIGItalizzazione delle aziende nel settore MANifatturiero"—PG/2018/631166, in the frame of the POR FESR 2014-2020 program of the Regione Emilia Romagna (Italy).

Conflicts of Interest: The authors declare no conflict of interest.

References

1. Schäufele, A.B.; Härdtl, K.H. Ferroelastic properties of lead zirconate titanate ceramics. *J. Am. Ceram. Soc.* **1996**, *79*, 2637–2640. [CrossRef]
2. Cordero, F.; Trequattrini, F.; Craciun, F.; Galassi, C. Octahedral tilting, monoclinic phase and the phase diagram of PZT. *J. Phys. Condens. Matter* **2011**, *23*, 415901. [CrossRef] [PubMed]
3. Roncari, E.; Galassi, C.; Craciun, F.; Capiani, C.; Piancastelli, A. A microstructural study of porous piezoelectric ceramics obtained by different methods. *J. Eur. Ceram. Soc.* **2001**, *21*, 409–417. [CrossRef]
4. RoHS Restricted Substances. Available online: https://www.rohsguide.com/rohs-substances.htm (accessed on 23 October 2022).
5. Galassi, C.; Roncari, E.; Capiani, C.; Fabbri, G.; Piancastelli, A.; Peselli, M.; Silvano, F. Processing of porous PZT materials for underwater acoustics. In *Proceedings of the Ferroelectrics*; Taylor & Francis Group: Abingdon, UK, 2002; Volume 268, pp. 47–52.
6. Roscow, J.; Zhang, Y.; Taylor, J.; Bowen, C.R. Porous ferroelectrics for energy harvesting applications. *Eur. Phys. J. Spec. Top.* **2015**, *224*, 2949–2966. [CrossRef]
7. Guo, R.; Wang, C.A.; Yang, A.K. Effects of pore size and orientation on dielectric and piezoelectric properties of 1-3 type porous PZT ceramics. *J. Eur. Ceram. Soc.* **2011**, *31*, 605–609. [CrossRef]
8. Rybyanets, A.N. Porous piezoelectric ceramics-a historical overview. In Proceedings of the Ferroelectrics, Edinburgh, UK, 9–12 August 2010; Volume 419, pp. 90–96.
9. Chen, C.; Wang, X.; Wang, Y.; Yang, D.; Yao, F.; Zhang, W.; Wang, B.; Sewvandi, G.A.; Yang, D.; Hu, D. Additive Manufacturing of Piezoelectric Materials. *Adv. Funct. Mater.* **2020**, *30*, 2005141. [CrossRef]
10. Venkataraman, N.; Rangarajan, S.; Harper, B.; Matthewson, M.J.; Safari, A.; Danforth, S.C. Process-property-performance relationship for fused deposition of ceramics (FDC) feedstock materials. *MRS Online Proc. Libr.* **2000**, *625*, 203. [CrossRef]
11. Allahverdi, M.; Danforth, S.; Jafari, M.; Safari, A. Processing of advanced electroceramic components by fused deposition technique. *J. Eur. Ceram. Soc.* **2001**, *21*, 1485–1490. [CrossRef]
12. Qiu, J.; Tani, J.; Yanada, N.; Kobayashi, Y.; Takahashi, H. Fabrication of Pb(Nb,Ni)O3-Pb(Zr,Ti)O3 piezoelectric ceramic fibers by extrusion of a sol-powder mixture. *J. Intell. Mater. Syst. Struct.* **2004**, *15*, 643–653. [CrossRef]
13. Turcu, S.; Jadidian, B.; Danforth, S.C.; Safari, A. Piezoelectric properties of novel oriented ceramic-polymer composites with 2-2 and 3-3 connectivity. *J. Electroceramics* **2002**, *9*, 165–171. [CrossRef]
14. Safari, A.; Akdogan, E.K. Rapid prototyping of novel piezoelectric composites. *Ferroelectrics* **2006**, *331*, 153–179. [CrossRef]
15. Sebastian, T.; Bach, M.; Geiger, A.; Lusiola, T.; Kozielski, L.; Clemens, F. Investigation of electromechanical properties on 3-d printed piezoelectric composite scaffold structures. *Materials* **2021**, *14*, 5927. [CrossRef] [PubMed]
16. Singh, P.; Smith, L.S.; Bezdecny, M.; Cheverton, M.; Brewer, J.A.; Venkataramani, V. Additive manufacturing of PZT-5H piezoceramic for ultrasound transducers. In Proceedings of the IEEE International Ultrasonics Symposium, IUS, Orlando, FL, USA, 18–21 October 2011; pp. 1111–1114.
17. Chen, Y.; Bao, X.; Wong, C.M.; Cheng, J.; Wu, H.; Song, H.; Ji, X.; Wu, S. PZT ceramics fabricated based on stereolithography for an ultrasound transducer array application. *Ceram. Int.* **2018**, *44*, 22725–22730. [CrossRef]

18. Hu, X.; Li, X.; Yan, K.; Qi, X.; Chen, W.; Wu, D. Fabrication of porous PZT ceramics using micro-stereolithography technology. *Ceram. Int.* **2021**, *47*, 32376–32381. [CrossRef]
19. Li, Y.Y.; Li, L.T.; Li, B. Direct ink writing of 3-3 piezoelectric composite. *J. Alloys Compd.* **2015**, *620*, 125–128. [CrossRef]
20. Hall, S.E.; Regis, J.E.; Renteria, A.; Chavez, L.A.; Delfin, L.; Vargas, S.; Haberman, M.R.; Espalin, D.; Wicker, R.; Lin, Y. Paste extrusion 3D printing and characterization of lead zirconate titanate piezoelectric ceramics. *Ceram. Int.* **2021**, *47*, 22042–22048. [CrossRef]
21. Chavez, L.A.; Ibave, P.; Wilburn, B.; Alexander, D.; Stewart, C.; Wicker, R.; Lin, Y. The Influence of Printing Parameters, Post-Processing, and Testing Conditions on the Properties of Binder Jetting Additive Manufactured Functional Ceramics. *Ceramics* **2020**, *3*, 65–77. [CrossRef]
22. Gureev, D.M.; Ruzhechko, R.V.; Shishkovskii, I.V. Selective laser sintering of PZT ceramic powders. *Tech. Phys. Lett.* **2000**, *26*, 262–264. [CrossRef]
23. Tarasova, E.; Juravleva, I.; Shishkovsky, I.; Ruzhechko, R. Layering laser-assisted sintering of functional graded porous PZT ceramoplasts. *Phase Transit.* **2013**, *86*, 1121–1129. [CrossRef]
24. Bernard, S.A.; Balla, V.K.; Bose, S.; Bandyopadhyay, A. Direct laser processing of bulk lead zirconate titanate ceramics. *Mater. Sci. Eng. B Solid-State Mater. Adv. Technol.* **2010**, *172*, 85–88. [CrossRef]
25. Diener, S.; Zocca, A.; Günster, J. Literature Review: Methods for achieving high powder bed densities in ceramic powder bed based additive manufacturing. *Open Ceram.* **2021**, *8*, 100191. [CrossRef]
26. Mariani, M.; Beltrami, R.; Brusa, P.; Galassi, C.; Ardito, R.; Lecis, N. 3D printing of fine alumina powders by binder jetting. *J. Eur. Ceram. Soc.* **2021**, *41*, 5307–5315. [CrossRef]
27. Du, W.C.; Ren, X.R.; Ma, C.; Pei, Z.J. Binder Jetting Additive Manufacturing of Ceramics: A Literature Review. In Proceedings of the ASME 2017 International Mechanical Engineering Congress and Exposition, Tampa, FL, USA, 3–9 October 2017; Volume 14.
28. Mariani, M.; Frias Blanco, G.; Mercadelli, E.; Sánchez-Herencia, A.J.; Galassi, C.; Lecis, N.; Ferrari, B. Tailoring α-alumina powder morphology through spray drying for cold consolidation by binder jetting. *Open Ceram.* **2022**, *12*, 100307. [CrossRef]
29. Mariani, M.; Beltrami, R.; Migliori, E.; Cangini, L.; Mercadelli, E.; Baldisserri, C.; Galassi, C.; Lecis, N. Additive manufacturing of lead-free KNN by binder jetting. *J. Eur. Ceram. Soc.* **2022**, *42*, 5598–5605. [CrossRef]
30. Gaytan, S.M.; Cadena, M.A.; Karim, H.; Delfin, D.; Lin, Y.; Espalin, D.; MacDonald, E.; Wicker, R.B. Fabrication of barium titanate by binder jetting additive manufacturing technology. *Ceram. Int.* **2015**, *41*, 6610–6619. [CrossRef]
31. Chavez, L.A.; Wilburn, B.R.; Ibave, P.; Delfin, L.C.; Vargas, S.; Diaz, H.; Fulgentes, C.; Renteria, A.; Regis, J.; Liu, Y.; et al. Fabrication and characterization of 3D printing induced orthotropic functional ceramics. *Smart Mater. Struct.* **2019**, *28*, 125007. [CrossRef]
32. Sufiiarov, V.; Kantyukov, A.; Popovich, A.; Sotov, A. Structure and properties of barium titanate lead-free piezoceramic manufactured by binder jetting process. *Materials* **2021**, *14*, 4419. [CrossRef]
33. Mercadelli, E.; Galassi, C. How to Make Porous Piezoelectrics? Review on Processing Strategies. *IEEE Trans. Ultrason. Ferroelectr. Freq. Control* **2021**, *68*, 217–228. [CrossRef]
34. Piazza, D.; Stoleriu, L.; Mitoseriu, L.; Stancu, A.; Galassi, C. Characterisation of porous PZT ceramics by first-order reversal curves (FORC) diagrams. *J. Eur. Ceram. Soc.* **2006**, *26*, 2959–2962. [CrossRef]
35. Piazza, D.; Capiani, C.; Galassi, C. Piezoceramic material with anisotropic graded porosity. *J. Eur. Ceram. Soc.* **2005**, *25*, 3075–3078. [CrossRef]
36. Gheorghiu, F.; Padurariu, L.; Airimioaei, M.; Curecheriu, L.; Ciomaga, C.; Padurariu, C.; Galassi, C.; Mitoseriu, L. Porosity-dependent properties of Nb-doped Pb(Zr,Ti)O3 ceramics. *J. Am. Ceram. Soc.* **2017**, *100*, 647–658. [CrossRef]
37. Padurariu, C.; Padurariu, L.; Curecheriu, L.; Ciomaga, C.; Horchidan, N.; Galassi, C.; Mitoseriu, L. Role of the pore interconnectivity on the dielectric, switching and tunability properties of PZTN ceramics. *Ceram. Int.* **2017**, *43*, 5767–5773. [CrossRef]
38. Marselli, S.; Pavia, V.; Galassi, C.; Roncari, E.; Craciun, F.; Guidarelli, G. Porous piezoelectric ceramic hydrophone. *J. Acoust. Soc. Am.* **1999**, *106*, 733–738. [CrossRef]
39. Roscow, J.I.; Pearce, H.; Khanbareh, H.; Kar-Narayan, S.; Bowen, C.R. Modified energy harvesting figures of merit for stress- and strain-driven piezoelectric systems. *Eur. Phys. J. Spec. Top.* **2019**, *228*, 1537–1554. [CrossRef]
40. Mariani, M.; Mariani, D.; De Gaudenzi, G.P.; Lecis, N. Effect of printing parameters on sintered WC-Co components by binder jetting. *Eur. J. Mater.* **2022**, *2*, 365–380. [CrossRef]
41. Lecis, N.; Mariani, M.; Beltrami, R.; Emanuelli, L.; Casati, R.; Vedani, M.; Molinari, A. Effects of process parameters, debinding and sintering on the microstructure of 316L stainless steel produced by binder jetting. *Mater. Sci. Eng. A* **2021**, *828*, 142108. [CrossRef]
42. Jiang, R.; Monteil, L.; Kimes, K.; Mostafaei, A.; Chmielus, M. Influence of powder type and binder saturation on binder jet 3D–printed and sintered Inconel 625 samples. *Int. J. Adv. Manuf. Technol.* **2021**, *116*, 3827–3838. [CrossRef]
43. Su, Z.; Zhao, K.; Ye, Z.; Cao, W.; Wang, X.; Liu, K.; Wang, Y.; Yang, L.; Dai, B.; Zhu, J. Overcoming the penetration–saturation trade-off in binder jet additive manufacturing via rapid in situ curing. *Addit. Manuf.* **2022**, *59*, 103157. [CrossRef]
44. Rahman, K.M.; Wei, A.; Miyanaji, H.; Williams, C.B. *Impact of Binder on Part Densification: Enhancing Binder Jetting Part Properties through the Fabrication of Shelled Geometries*; Elsevier: Amsterdam, The Netherlands, 2023; Volume 62.
45. Miao, G.; Moghadasi, M.; Li, M.; Pei, Z.; Ma, C. Binder Jetting Additive Manufacturing: Powder Packing in Shell Printing. *J. Manuf. Mater. Process.* **2022**, *7*, 4. [CrossRef]

46. Bowen, C.R.; Perry, A.; Lewis, A.C.F.; Kara, H. Processing and properties of porous piezoelectric materials with high hydrostatic figures of merit. *J. Eur. Ceram. Soc.* **2004**, *24*, 541–545. [CrossRef]
47. Guo, R.; Wang, C.A.; Yang, A. Piezoelectric properties of the 1-3 type porous lead zirconate titanate ceramics. *J. Am. Ceram. Soc.* **2011**, *94*, 1794–1799. [CrossRef]
48. Zhang, Y.; Xie, M.; Roscow, J.; Bao, Y.; Zhou, K.; Zhang, D.; Bowen, C.R. Enhanced pyroelectric and piezoelectric properties of PZT with aligned porosity for energy harvesting applications. *J. Mater. Chem. A* **2017**, *5*, 6569–6580. [CrossRef] [PubMed]